The flow fields involved in hydrodynamic imaging by blind Mexican cave fish (*Astyanax fasciatus*). Part I: open water and heading towards a wall

Shane P. Windsor*, Stuart E. Norris, Stuart M. Cameron, Gordon D. Mallinson and John C. Montgomery

School of Biological Sciences, University of Auckland, Private Bag 92019, Auckland 1142, New Zealand

*Author for correspondence at present address: University of Oxford, Department of Zoology, Tinbergen Building, South Parks Road, Oxford OX1 3PS, UK (shane.windsor@zoo.ox.ac.uk)

SUMMARY

Blind Mexican cave fish (*Astyanax fasciatus*) sense the presence of nearby objects by sensing changes in the water flow around their body. The information available to the fish using this hydrodynamic imaging ability depends on the properties of the flow field it generates while gliding and how this flow field is altered by the presence of objects. Here, we used particle image velocimetry to measure the flow fields around gliding blind cave fish as they moved through open water and when heading towards a wall. These measurements, combined with computational fluid dynamics models, were used to estimate the stimulus to the lateral line system of the fish. Our results showed that there was a high-pressure region around the nose of the fish, low-pressure regions corresponding to accelerated flow around the widest part of the body and a thick laminar boundary layer down the body. When approaching a wall head-on, the changes in the stimulus to the lateral line were confined to approximately the first 20% of the body. Assuming that the fish are sensitive to a certain relative change in lateral line stimuli, it was found that swimming at higher Reynolds numbers slightly decreased the distance at which the fish could detect a wall when approaching head-on, which is the opposite to what has previously been expected. However, when the effects of environmental noise are considered, swimming at higher speed may improve the signal to noise ratio of the stimulus to the lateral line.

Key words: *Astyanax fasciatus*, biomechanics, blind cave fish, computational fluid dynamics, hydrodynamic imaging, lateral line.

INTRODUCTION

Fish have the potential to be able to sense their surroundings by sensing changes in the flow fields generated around their bodies as they swim through the water. Fish are able to get information about nearby objects by sensing the changes the presence of objects cause in the flow field; this is known as hydrodynamic imaging (Hassan, 1989). This is best known to be used by the hypogean (cave-dwelling) form of *Astyanax fasciatus* Cuvier 1819, commonly known as the blind Mexican cave fish (von Campenhausen et al., 1981; Weissert and von Campenhausen, 1981).

Fish are able to sense water motion using their lateral line mechanosensory system. The lateral line is composed of individual sensory organs called neuromasts. Each neuromast is composed of a group of hair cells that project their sensory cilia into a gelatinous cupula. When the cupula is displaced by motion of the surrounding fluid the hair cells are stimulated, sending information to the central nervous system. There are two sub-systems of neuromasts, which make up the lateral line. Superficial neuromasts are located on the surface of the skin and their cupula are displaced in proportion to the velocity of the flow, encoding the velocity component of the flow field (Kalmijn, 1988). Canal neuromasts sit in canals under the surface of the skin and are located between pores that open to the surrounding water. The cupula of canal neuromasts are displaced in proportion to the difference in pressure between the pores to either side, encoding the gradient of the pressure component of the flow field (Denton and Gray, 1983; Denton and Gray, 1988). For a full review of the lateral line system, see Coombs and Montgomery (Coombs and Montgomery, 1999).

In order to understand how fish use flow-field distortions to sense their surroundings it is necessary to understand the nature of the flow field around the fish and how the flow field is altered by the presence of objects. It is then possible to estimate how these changes may be encoded by the lateral line. Blind cave fish are the most recognised species of fish that are known to use hydrodynamic imaging, but it is highly likely that other fish species also have this ability. Numerous studies using experimentally blinded fish of other species have observed blinded fish avoiding obstacles without touching them (Dijkgraaf, 1963; Partridge and Pitcher, 1980; Teyke, 1988; Yasuda, 1973), presumably by using hydrodynamic imaging. Hydrodynamic imaging appears to be most effective when fish are gliding with their body held straight; blind cave fish spend approximately 70% of their time gliding (Windsor et al., 2008). Hence it is the flow field around fish when gliding that is of most interest when studying hydrodynamic imaging.

There is a considerable amount known about the flow fields involved with the propulsion of fish (for a review, see Drucker and Lauder, 2002), but surprisingly little about the flow fields around gliding fish. Dubois et al. fitted live bluefish (*Pomatomus saltatrix*) with Pitot pressure tubes and measured the pressure fields on the body surface of the fish as they swam (Dubois et al., 1974). A stagnation point was found at the jaw of the fish, with positive pressure at the front of the fish, becoming negative as the width of the body increased and then becoming positive again towards the tail. Kuiper also briefly examined the pressure distribution around a fish-shaped model using a Pitot pressure tap system and found a similarly shaped pressure variation along the body (Kuiper, 1967).

The stimulus to the lateral line generated by the hydrodynamic interaction of a three-dimensional (3-D) fish shape and a flat surface has been investigated in a series of mathematical modelling studies by Hassan (Hassan, 1985; Hassan, 1992a; Hassan, 1992b). These studies were based on potential flow modelling, which simulates flows at very high Reynolds numbers (*Re*). In potential flow models,

the fluid is assumed to be inviscid and, as such, viscous boundary layers are not modelled. This may be a major limitation in these models, as the presence of viscous boundary layers could be expected to have a large impact on the form of the flow field around a small fish at low *Re* and, hence, the effective stimulus to the lateral line.

The objectives of this study were to determine the available stimulus to the lateral line by measuring the flow fields around gliding blind cave fish, and to determine how these flow fields were altered through interactions with external surfaces. The flow fields around cave fish gliding through open water and gliding head-on towards a wall were measured experimentally using particle image velocimetry (PIV). Measured flow fields were used to validate computational fluid dynamic (CFD) models constructed for these same situations. These models were then used to estimate the lateral line stimulus. In a companion paper the flow fields around fish gliding parallel to a wall were studied using similar techniques (Windsor et al., 2010). The kinematics and behaviour of blind cave fish in these same situations has previously been measured in detail (Windsor et al., 2008), allowing comparisons to be made between the behaviour of the fish and the sensory information that is potentially available.

MATERIALS AND METHODS
Fish
Blind Mexican cave fish were purchased from a commercial aquarium supplier. The fish ranged in size from 40 to 60 mm in total length, with a mean (±s.e.m.) length of 44±4 mm. The fish were housed as described previously (Windsor et al., 2008). All experiments were carried out in accordance with the animal care policy of the University of Auckland.

Experimental procedure
PIV measurements were made of individual fish swimming freely in a glass experimental tank measuring 400 mm×300 mm×80 mm (length × breadth × height: Fig. 1). The tank had a short partition midway down the longer wall to direct the fish to swim across the tank, head-on toward a submerged wall on the opposite side of the tank. The top of this wall was slightly below the surface of the water in order to prevent optical distortions created by any meniscus at the surface. The PIV system was set up to look directly down this wall, midway along the tank in a horizontal plane 10 mm above the tank bottom for smaller fish (<50 mm in length), or 15 mm above the bottom for larger fish (>50 mm in length). The field of view of the PIV camera was 23 mm×23 mm. Two additional cameras (Marlin F131B, AVT, Stadtroda, Germany) were also used to record the fish's behaviour before and after it passed through the field of view of the PIV camera and to record the height at which the fish swam through the laser sheet. The length of the trials was limited to 9 min by the capacity of the computer hard disk drive array recording the PIV images. The water in the experimental tank was completely still apart from the motion generated by the movement of the fish. Between trials an aerator and heater were placed in the experimental tank to maintain the temperature (25°C) and oxygen level of the water.

The particle image velocimetry system
PIV measurements were made using a custom built PIV system (Schlicke et al., 2007). The system used an oscillating mirror driven by a galvanometer in combination with a continuous laser (5 W 532 nm Nd:YVO4 laser, Spectra-Physics Millenia, Santa Clara, CA, USA) to generate a laser light sheet approximately 1 mm thick. The PIV camera (Basler A504k, Ahrensburg, Germany) captured 8 bit
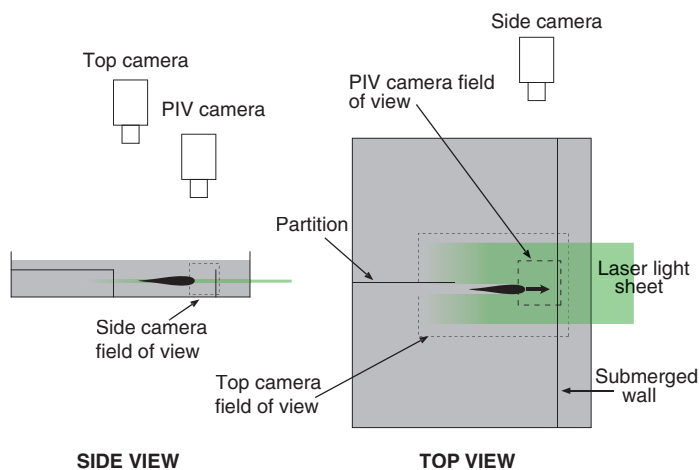

Fig. 1. Diagram of experimental setup for particle image velocimetry (PIV) measurements (not to scale). A partition in the middle of the tank directed the fish to approach the submerged wall on the opposite side of the tank. The PIV camera recorded the motion of particles in the laser light sheet, and the movements of the fish were recorded from above and from the side by two additional cameras.

monochrome 960×960 pixel images at 200 frames s^{-1}. The water was seeded with neutrally buoyant 10 μm diameter hollow glass spheres.

Particle image velocimetry processing
Each PIV video sequence was reviewed before processing and only passes where a fish was gliding in still water, in a straight line, with no noticeable pitch or roll relative to the laser plane were analysed. In addition, only passes where the laser sheet visibly intersected a fish mid way up the dorsal–ventral axis without reflection were considered, in order to minimise any out of plane flows. Full 3-D CFD modelling studies of swimming giant danio (*Danio malabaricus*) have shown that the flow field is strongly two-dimensional (2-D) along the mid body plane of this similarly shaped fish (Wolfgang et al., 1999).

A series of image processing procedures was performed using custom written software (Cameron, 2007) before calculating the velocity vector field. Any glare around the fish was removed by subtracting a median filtered copy of the image. The edge of the fish intersecting the laser sheet was then detected using an intensity-gradient-based Canny edge detector and the body of the fish was masked out by mirroring this edge about the mid-line of the fish.

The flow velocity field was calculated from the processed images using an iterative cross-correlation algorithm with a final interrogation window of 32×32 pixels with a 50% window overlap, giving a 60×60 field of velocity vectors. The cross-correlation algorithm utilised a continuous-window shift with a linear velocity gradient correction to compensate for the steep velocity gradients in the boundary layer around the fish. The total estimated error of the PIV system and the cross-correlation methods used was approximately ±1% (Cameron, 2007). Velocity vectors were not calculated for any interrogation regions that overlapped the body of the fish in order to avoid erroneous vectors. The velocity of a fish was calculated by cross-correlating images of its outline.

The interpretation of the velocity field was also aided by making artificial particle streak images from the PIV video sequences. This was done by thresholding each PIV image to create a binary image and then segmenting out the body of the fish. This left only the

brightest particles in the image. Series of consecutive frames were then added together to form particle streak images, which showed the structure of the velocity field. The particle streak images were particularly effective in visualising the boundary layer flow close to the fish, whereas the PIV velocity vectors did not have sufficient resolution to do so.

Pressure field calculation

As the lateral line is capable of sensing both the velocity and pressure gradient of the surrounding fluid flow, it was desirable to measure both the velocity and pressure components of the flows around the fish. PIV is traditionally only used to measure the velocity field, but it is also possible to estimate the pressure field from the velocity field using the Poisson pressure relationship (Fujisawa et al., 2004; Fujisawa et al., 2006; Fujisawa et al., 2005; Gurka et al., 1999; Hosokawa et al., 2003; Murai et al., 2007). A finite difference approach was used, with the pressure gradient field being calculated from experimental velocity data using the Navier–Stokes equations. This was then related to the pressure distribution using a pressure Poisson equation [see Windsor (Windsor, 2008) for a full description]. In this process it was assumed that at any particular instant the velocity field was quasi-steady, i.e. the fish was not accelerating or decelerating significantly. All PIV measurements were made as the fish decelerated smoothly while gliding. Based on previous kinematic measurements (Windsor et al., 2008) the mean change in fish velocity between video frames would have only been approximately –0.40% of the swimming velocity of the fish. It was also assumed that the flow was laminar with no out of plane flow (divergence free in a 2-D sense). All the flows observed in the PIV experiments were laminar with no indications of turbulence.

Stimulus estimation

The stimulus to the superficial neuromasts is generally considered to be the velocity of the flow past each neuromast (Kroese and Schellart, 1992). However, this is complicated by the fact that the cupula is buried within the boundary layer flow on the surface of the fish, and in this region the velocity of the flow changes rapidly with distance from the surface (Jielof et al., 1952; Kalmijn, 1988; Kalmijn, 1989). A superficial neuromast has a cupula that is 100–180 μm long (Teyke, 1990), and responds in proportion to the fluid forces acting on the cupula as a whole (McHenry et al., 2008). As such there is no obvious distance above the skin surface at which to measure the velocity of the flow. A good approximation of the magnitude of the stimulus to the superficial neuromasts is the wall shear stress (τ_w) (Rapo et al., 2009; Windsor and McHenry, 2009) on the surface of the fish:

$$\tau_w = \mu \left(\frac{\partial \mathbf{u}_t}{\partial y} \right) \bigg|_{y=0}, \tag{1}$$

where $\mathbf{u}_t$ is the tangential velocity, y is the direction normal to the surface and μ is the dynamic viscosity of the fluid. The wall shear stress is proportional to the difference in velocity between the surface of the fish and the fluid surrounding the neuromast. In regions close to the body where the flow velocity is high, the wall shear stress will be high, and in regions where the velocity is low, the wall shear stress will be low. The normalised version of the shear stress is the skin friction coefficient (C_f) given by:

$$C_f = \frac{\tau_w}{0.5 \rho U^2}, \tag{2}$$

where ρ is the density of the fluid and U is swimming speed of the fish, or in the reference frame of the fish, the speed of the oncoming

uniform flow. The superficial neuromasts are distributed in high densities all over the body of blind cave fish, so the superficial neuromasts were assumed to encode the shear stress at every point on the body of the fish.

The stimulus to the canal neuromasts is the difference in pressure between adjacent canal pores (Denton and Gray, 1983; Kalmijn, 1988). The canal pores were assumed to be spaced at 2% body length (BL) intervals based on morphological drawings of blind cave fish (Schemmel, 1967). The stimulus to the first neuromast between the pores 0.02 and 0.04 BL down the fish is plotted as the stimulus at 0.02 BL. The position of the stimuli on the body was measured against the distance along the surface of the fish from the nose.

To aid in the comparison of flow fields at different Re, the pressure (P) and velocity (**u**) fields were normalised. The velocity field was normalised with respect to the velocity of the fish:

$$U_{\text{norm}} = \frac{|\mathbf{u}|}{U}. \tag{3}$$

The coefficient of pressure (C_P) was used to represent the normalised pressure field:

$$C_P = \frac{P}{0.5 \rho U^2}. \tag{4}$$

The stimulus to the neuromasts of the lateral line system was estimated based on the same flow field variables for both the PIV measurements and the CFD models.

Particle image velocimetry limitations

The PIV measurements of the flow field around the fish had a number of limitations. It was difficult to measure the velocity field very close to the body of the fish, as interrogation regions that overlapped the body, had to be treated as part of the fish; otherwise erroneous velocity vectors were calculated. This, coupled with the comparatively large spacing of the velocity vectors (0.38 mm) relative to the thickness of the boundary layer meant that it was not possible to extract the shear stress distribution on the surface of the fish. The accurate estimation of the pressure field at the edge of the fish was also limited by the resolution of the velocity vectors close to the body of the fish and by the boundary conditions that had to be applied in the numerical algorithm for solving the Poisson equation for pressure. The influence of the numerical approximations to these boundary conditions were extensively tested (Windsor, 2008), and when combined with experimental measurement noise were estimated to introduce a mean (±s.d.) error of approximately 6±2% to the calculated pressure values at the boundary of the fish.

Overall, the PIV measurements gave a good representation of the general form of the flow field away from the body surface of the fish. At the surface of the fish, where we were interested in the stimulus to the lateral line, the PIV measurements were limited by the spatial resolution of the velocity vectors. For this reason, the experimental PIV measurements were used to validate the results of CFD models in regions of the flow away from the body, and the CFD models were then used to simulate the flows at the surface of the fish and to estimate the stimuli to the lateral line.

Open water computational fluid dynamic modelling

Two 2-D CFD models and a 3-D model were used to model a fish gliding through open water (Fig. 2). The first 2-D model was based on a NACA 0013 aerofoil, which has the same length to maximum width ratio as a blind cave fish. The second 2-D model was a 'fish shaped' model representing the cross-sectional shape of the blind cave fish, as seen when looking down at the dorsal surface of the
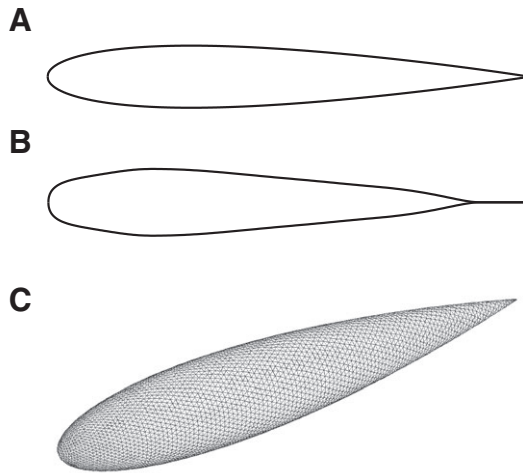
A

B

C

Fig. 2. Diagram of the body shapes used in the computational fluid dynamics (CFD) models. (A) 2-D NACA 0013 aerofoil. (B) 2-D fish shape. (C) 3-D axisymmetric body of revolution based on a NACA 0013 aerofoil.
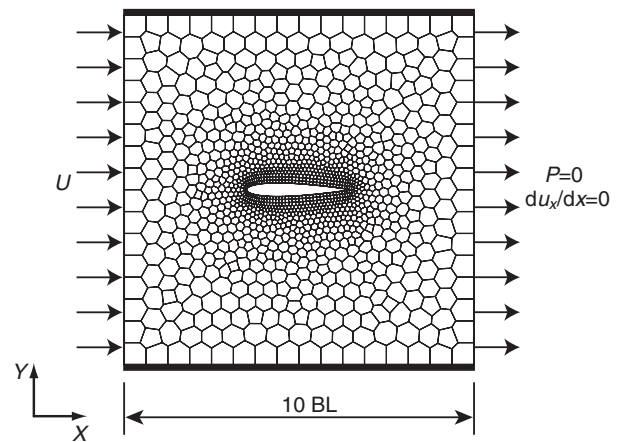

Fig. 3. Diagram of the 2-D CFD mesh and boundary conditions (not to scale). The body of the fish was in the centre of the domain, with the nose of the fish at the origin and the body aligned with the *X*-axis. The −*X* face of the domain was an inlet, with a uniform inlet velocity based on the Reynolds number (*Re*). The +*X* face of the domain was set as an outlet, with the pressure set to zero and a zero velocity gradient normal to the boundary. The +*Y* and −*Y* faces were set as symmetry planes. The fish geometry was set as a no slip wall. A very coarse representative mesh is shown. The mesh had structured inflation layers around the fish, while the rest of the domain was filled with an unstructured Voronoi mesh.

fish. The shape of the fish was traced from video frames of gliding blind cave fish. For the 3-D modelling, an axisymmetric body of revolution based on a NACA 0013 aerofoil, was used to represent the shape of the fish. This shape matched the medial–lateral cross-sectional shape of the fish well (excluding the tail), but did not have the increased dorsal–ventral height seen in blind cave fish. This shape represented the other extreme of geometry from a two-dimensional aerofoil. The true fish shape, with its flattened lateral surfaces, lies somewhere between the torpedo shaped body of revolution and the infinite wing being modelled in the 2-D cases. The 3-D model showed the effects of flow in the dorsal–ventral direction, although these effects will have been exaggerated compared with the true shape of the fish. The models were run at *Re* ranging from 1000 to 8000, representing the *Re* range observed in previous behavioural trials (Windsor et al., 2008). This corresponded to swimming velocities ranging from 23 to 180 mm s^{-1} for a fish of the mean length used in the PIV trials. The *Re* was defined based on the body length of the fish (*L*):

$$Re = \frac{UL\rho}{\mu}. \tag{5}$$

In the 2-D models (Fig. 3), the boundaries of the square flow domain were placed 5 BL away from the centre of the fish, giving a domain size of 10×10 BL (*X*×*Y*), with 64 nodes along each boundary face. A mesh was created around the fish with 256 nodes along each surface, with nodes bunched around the leading and trailing edges of the body, to give a higher mesh resolution in these areas. The mesh had 20 structured inflation layers around the fish, so as to accurately capture the boundary layer flow. The rest of the domain was filled by an unstructured Voronoi mesh. For the 3-D open water model a similar geometry was used, with the domain being 10 BL in the *Z* dimension and with 20 nodes along each boundary face. A mesh was created around the fish with 128 nodes along the length of the fish and 10 structured inflation layers around the fish.

All modelling was done using the CFD code (Norris et al., 2010; Were, 1997). The incompressible Navier–Stokes equations were solved on an unstructured mesh using a scheme that was formally third order in space and first order in time. See the Appendix for full details of the CFD methodology used. The flow was assumed to be laminar given the low *Re* being modelled.

Mesh refinement studies were conducted to establish the mesh resolution needed to accurately capture the nature of the flow field and quantify the discretisation error. For the 2-D modelling, a NACA 0008 aerofoil at a *Re* of 6000 was used as a test case, for the 3-D modelling the axisymmetric body of revolution based on a NACA 0013 aerofoil was used. In both cases a range of mesh resolutions were tested and the results on each mesh compared using Richardson extrapolation (Roache, 1997). See Appendix for full details and results.
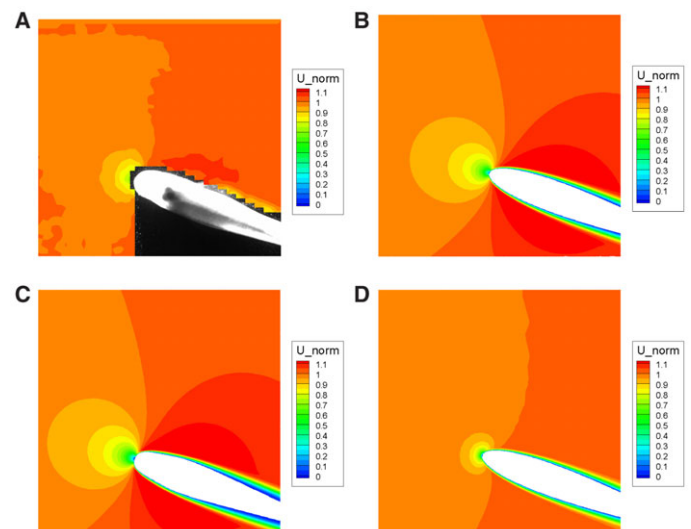

Fig. 4. Contour plots of the normalised absolute velocity fields (*U*$_{norm}$) in open water at a *Re* of 6000. (A) PIV velocity field, with the wall of the tank at the top of the frame. The shadow of the fish obscures the flow field on the far side of the fish. Fish body length is 49 mm. (B) 2-D NACA 0013 CFD velocity field. (C) 2-D fish-shaped CFD velocity field. (D) 3-D NACA 0013 body CFD velocity field. The CFD plots are shown in the same orientation as the PIV data to facilitate comparison.
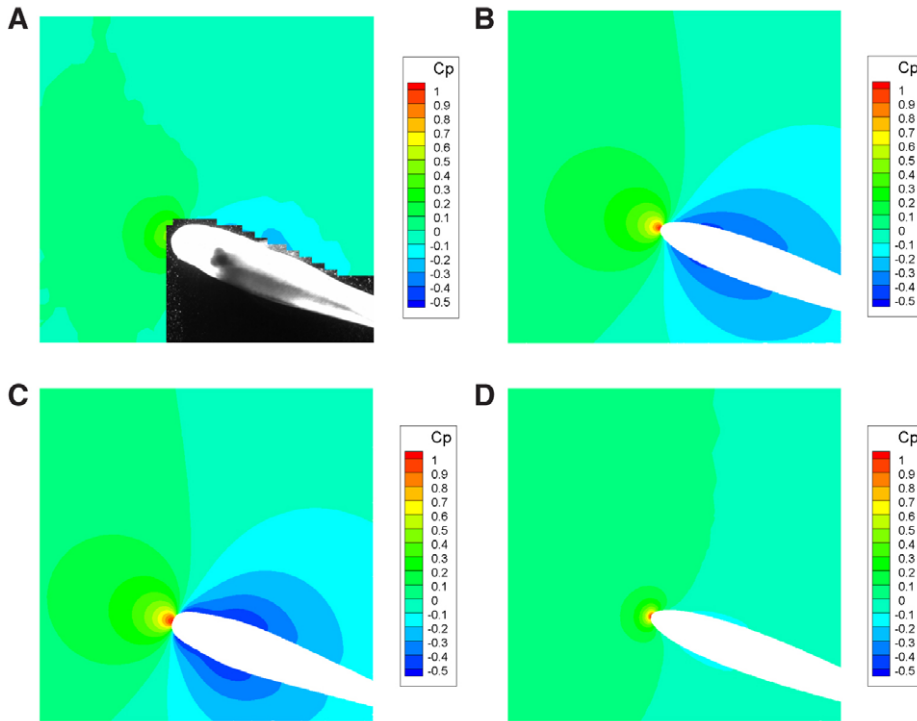
Fig. 5. Contour plots of the coefficient of pressure (C_P) in open water at a *Re* of 6000. (A) Estimated normalised PIV pressure field for the same pass as shown in Fig. 4A. (B) 2-D NACA 0013 CFD pressure field. (C) 2-D fish-shaped CFD pressure field. (D) 3-D NACA 0013 body CFD pressure field. The CFD plots are shown in the same orientation as the PIV data to facilitate comparison.

Head-on computational fluid dynamic modelling

To model the head-on approach of a body towards a wall required the geometry of the model to change as the body moved towards the wall. This was implemented in the ALE CFD software using a smoothly deforming unstructured Voronoi mesh, where the boundary nodes of the mesh moved through a defined motion over time. Within the mesh, the internal nodes were moved using an iterative smoothing algorithm, and the connectivity of the nodes recalculated at each step to maintain a valid Voronoi mesh. The Navier–Stokes equations were cast in the arbitrary Lagrangian Eulerian (ALE) form (Hirt et al., 1974) to enable the flow to be solved on a moving mesh. See Norris et al. for the full details of the ALE method used (Norris et al., 2010).

The same two 2-D shapes as in the open water model were used to represent the body of a fish: a NACA 0013 aerofoil and a fish shaped geometry. The flow domain was a square, 10×10 BL ($X \times Y$) in size, with the $-X$ face of the domain representing a solid wall. The solution process was started with the body aligned along the X-axis, 6 BL away from the $-X$ boundary. The body was then moved steadily towards the wall as the solution progressed, up to the point where the nose of the body was so close to the wall that the formation of a valid mesh was no longer possible. All of the boundaries of the domain were set as no slip walls. The fish body was set as a no slip wall with a prescribed velocity of 1 BL per unit time.

There were 256 nodes along each side of the fish body, with nodes bunched around the leading and trailing edges of the body to give a higher mesh resolution in these areas. There were 10 structured inflation layers around the body so as to accurately capture the boundary layer flow. The body approached the $-X$ boundary wall, which had 736 nodes, with the nodes being bunched around the point where the nose of the body would hit the wall. The $+Y$ and $-Y$ boundaries each had 56 nodes, bunched towards the $-X$ face, and the $+X$ boundary had 32 nodes. The domain was filled with an unstructured Voronoi mesh.

Models were run at *Re* of 1000, 2000, 4000 and 6000. The mean *Re* measured for head-on approaches in previous behavioural experiments was 3000±200 with a range from 960 to 7900 (Windsor et al., 2008). The same time step and body velocity were used in all of the models, with the viscosity of the fluid being varied to alter the *Re*. The time step for each iteration was constant and set to keep the maximum Courant number less than 0.4, in order to maintain the stability and accuracy of the solution (Anderson, 1995). The effect of the size of the time step was quantified (see Appendix for full details). The flow was assumed to be laminar given the low *Re* being modelled. The pressure at one node, well away from the region of interest, was set to zero in order to define a reference pressure for the pressure field.

To verify the implementation of the ALE-based moving mesh, the moving mesh solution was compared with the open water NACA 0013 model at a *Re* of 6000. See Appendix for full details and results. It was found that once the body had moved 4 BL then the pressure distribution was steady and that over the final 2 BL as it approached the wall, any changes to the flow field were due to the presence of the wall.

RESULTS
Open water results

The flow fields measured using PIV showed a characteristic pattern when the fish were gliding through open water well away from the wall (Fig. 4A). In the frame of reference of the moving fish there was a stagnation point at the nose of the fish, where the flow velocity was zero relative to the fish. Down the side of the fish there was a region of accelerated flow, which reached a maximum close to the widest part of the body of the fish. Beyond the widest point the edges of a boundary layer could be seen. Here the fluid was being entrained and moving along with the fish. This was seen as a region of decelerated flow, growing in size down the fish. The pressure field calculated from the velocity field can be seen in Fig. 5A. The stagnation point corresponds with the region of high pressure at the nose of the fish. The accelerated flow corresponds with the region of low pressure down the side of the fish. As pressure is constant

across a boundary layer (White, 2006) this feature of the flow could not be identified in the pressure field. All the flows observed in the PIV experiments were laminar with no indications of turbulence.

The CFD velocity fields around the 2-D NACA 0013 aerofoil and the 2-D fish shape were very similar to each other (Fig. 4B,C). They both showed a large area of reduced velocity in front of the fish and large areas of accelerated flow down the sides of the fish. In comparison, the 3-D aerofoil CFD model (Fig. 4D) showed a much smaller region of reduced velocity in front of the nose and no part of the flow was accelerated above the free stream velocity. The PIV results indicate that the flow around the fish fell between the 2-D and 3-D cases. The CFD models all showed boundary layers of a similar thickness, and the PIV results also suggested the edge of a boundary layer of a similar thickness. The pressure fields showed similar trends to the velocity fields (Fig. 5B,C,D). Both 2-D CFD models showed large high-pressure regions at the nose, as well as large low-pressure regions down the sides of the body. The fish shape had slightly larger high- and low-pressure regions than the aerofoil. The 3-D model again showed much smaller high- and low-pressure regions, reflecting the smaller accelerations seen in the velocity field. The PIV data again fell between the 2-D and 3-D CFD modelling results.

The pressure fields calculated from the open water PIV velocity fields were compared with those calculated in the different CFD models (Fig. 6). Unlike the CFD, the PIV measurements did not capture the stagnation point at the tip of the nose, with a mean C_P of approximately 0.5 compared with the value of 1.0 predicted by hydrodynamic theory. This is likely to be due to PIV being unable to measure the velocity of the flows very close to the body surface; the high pressure gradients normal to the body at the stagnation point mean that the off body pressure calculated from the PIV data is not representative of the surface pressure. The low stagnation point pressure predicted by the PIV means that the estimated pressure gradient stimulus to the canal neuromasts at the nose of the fish were less than those calculated in the CFD models. Beyond 0.1 BL down the side of the fish, the PIV showed negative pressure regions that lay between the 2-D and 3-D aerofoil CFD model results. The CFD results indicate that the pressure gradient normal to the body surface is moderate in these regions, which suggests that the off body pressure captured by the PIV is more representative of the surface pressures away from the nose. The shear stress distribution could not be
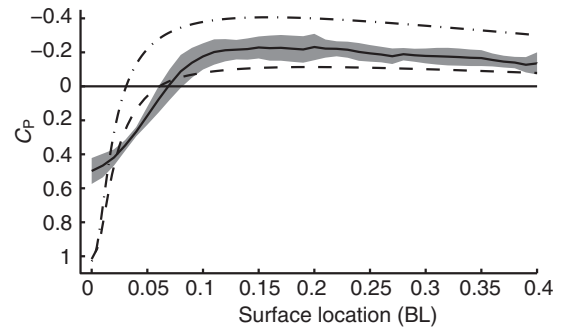

Fig. 6. PIV and CFD open water normalised pressure (C_P) distributions at a Re of 6000. The solid black line is the mean of five PIV passes at Re of approximately 6000, with the 95% confidence interval shown by the grey shading. The dashed line is the normalised pressure distribution on the NACA 0013 3-D model as calculated in the CFD model, the dot-dash line is for the NACA 0013 2-D model. Note that the C_P distribution is plotted with the Y-axis inverted in the aerodynamic convention. All distributions are shown only for the first 0.4 BL of the fish, as the PIV measurements further down the body were obscured by the pectoral fin.

estimated from the PIV data because of the limited resolution of the PIV velocity vectors close to the body of the fish.

The CFD models showed the effect of body shape on the lateral line stimuli (Fig. 7). The pressure distributions of the NACA aerofoils had similar shapes, but the 3-D model had a lower magnitude negative pressure region down the sides and full pressure recovery, with a slightly positive pressure at the trailing edge, while the 2-D aerofoil still had a significantly negative pressure at this point. The shapes of the shear stress distributions were also similar, with the 3-D model having a slightly decreased peak shear stress near the nose and a higher shear stress down the rear of the fish. The pressure distribution on the 2-D fish shape and the 2-D aerofoil were similar in magnitude, but the more complex curvature of the fish shape affected the shape of the pressure distribution. The dip following the pressure peak corresponded to a change in curvature where the fish shape flattened out slightly. A similar effect from this flattening could be seen in the shear distribution. The model of Hassan shows a very different pressure distribution to all of the
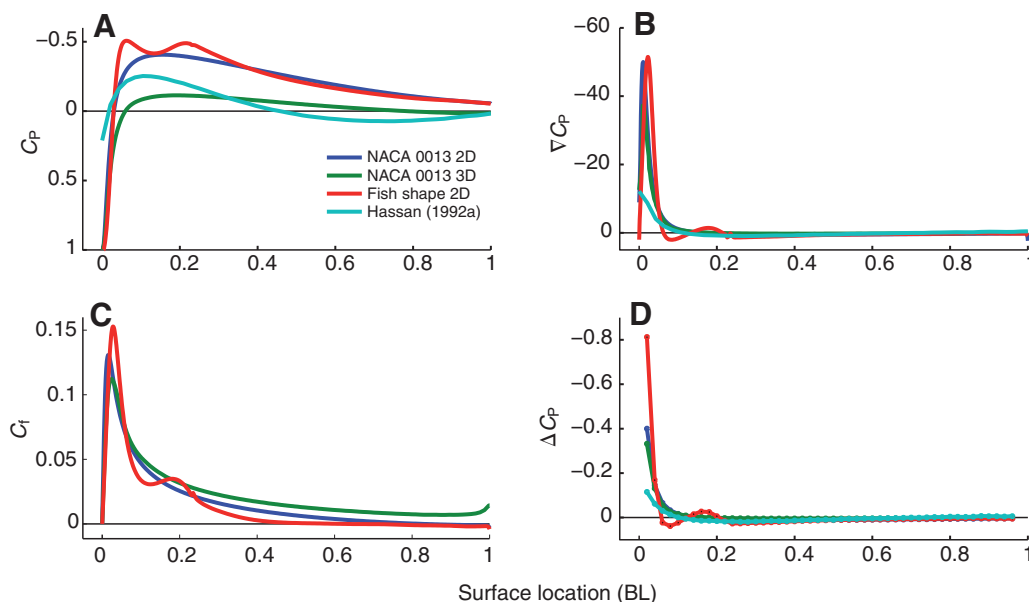

Fig. 7. CFD results showing the effect of body shape on the lateral line stimuli in open water at a Re of 6000. (A) Normalised pressure (C_P) distributions. (B) Normalised pressure gradient (∇C_P) distribution. (C) Normalised shear stress (C_f) distributions. The shear stress distribution was not calculated in Hassan's model. (D) Normalised pressure differences across pores (ΔC_P) at 2% body length (BL) spacing. Note that the C_P distributions in panels A, B and D are plotted with the Y-axis inverted in the aerodynamic convention, so a negative pressure difference means a more positive pressure at the rostral pore.

CFD models, with positive pressure down the rear half of the fish (Hassan, 1992a). In terms of the normalised pressure difference across the canal pores, the maximum stimuli at the nose in Hassan's model were only 35% of that predicted by the 3-D CFD model, the closest comparison in terms of geometry. As Hassan's model was inviscid, it was not possible to compare the shear stress distributions.

Head-on results

As fish glided head-on towards a wall the PIV video sequences showed a characteristic pattern of changes in the flow field in front of the fish. Looking at the flow from the point of view of a stationary observer, as the fish approached the wall the fluid was pushed out to both sides of the nose, moving parallel with the wall (Fig. 8), and the pressure at the stagnation point at the nose of the fish increased. The 2-D CFD head-on models and the PIV results showed similar velocity distributions as the fish neared the wall (Fig. 9). The CFD models showed that, when the body was more than about 0.30 BL from the wall, there was a region of fluid at the nose that was pushed in front of the fish (Fig. 10). As the body got closer to the wall the fluid in front of the fish began to be pushed increasingly to both sides of the nose because of the presence of the wall. When the body closed to within 0.10 BL of the wall, the velocity of the flow immediately in front of the nose began to rapidly increase. The width of the boundary layer on the body remained relatively constant as the body approached the wall. The pressure field showed a similar pattern to the velocity field, with the maximum C_P at the stagnation point at the nose of the fish rapidly increasing from 1 when the body was 0.30 BL from the wall, to over 4 when the body was 0.02 BL from the wall. However, the pressure field down the body of the fish remained relatively constant as the body approached the wall. The changes to the pressure and velocity fields around the fish-shaped model were very similar to those around the aerofoil, except for the broader nose of the fish-shaped body creating larger magnitude changes in the flow around the nose as the body came within 0.10 BL of the wall.

The stimuli to both the canal and superficial neuromasts increased rapidly at the nose of the fish as it approached the wall and there was relatively little change over the rest of the body (Fig. 11). The changes in both the superficial and canal stimuli were confined to approximately the first 0.20 BL along the body surface. In behavioural experiments blind cave fish detected the presence of a wall directly in front of them when they were 0.11±0.01 BL away, swimming at a mean Re of 3000±200 (Windsor et al., 2008).

As the Re increased, the thickness of the boundary layer around the body decreased (see Windsor and McHenry, 2009), and for Re above 6000, vortex shedding occurred at the trailing edge. This vortex shedding did not affect the lateral line stimulus around the head of the fish. With increasing Re, there was a small decrease in the distance at which the fish would detect the wall if it was assumed that the fish could detect a certain level of relative change in lateral line stimuli (Fig. 12). In terms of the time the fish had to change course after detecting the wall, the effect of the changes in the detection distance due to Re effects was small in comparison with the effect of swimming speed. For example, assuming a relative sensitivity threshold of 0.20, the same fish swimming at a Re of 6000 would have a 7.2-fold decrease in the time available to change course in comparison with when swimming at a Re of 1000. Only 3% of the decrease in available time would result from the difference in detection distance, leaving almost all of the decrease being simply due to the fish swimming faster.

The PIV experiments and modelling were conducted in still water with no environmental noise. To give an indication of the effect of
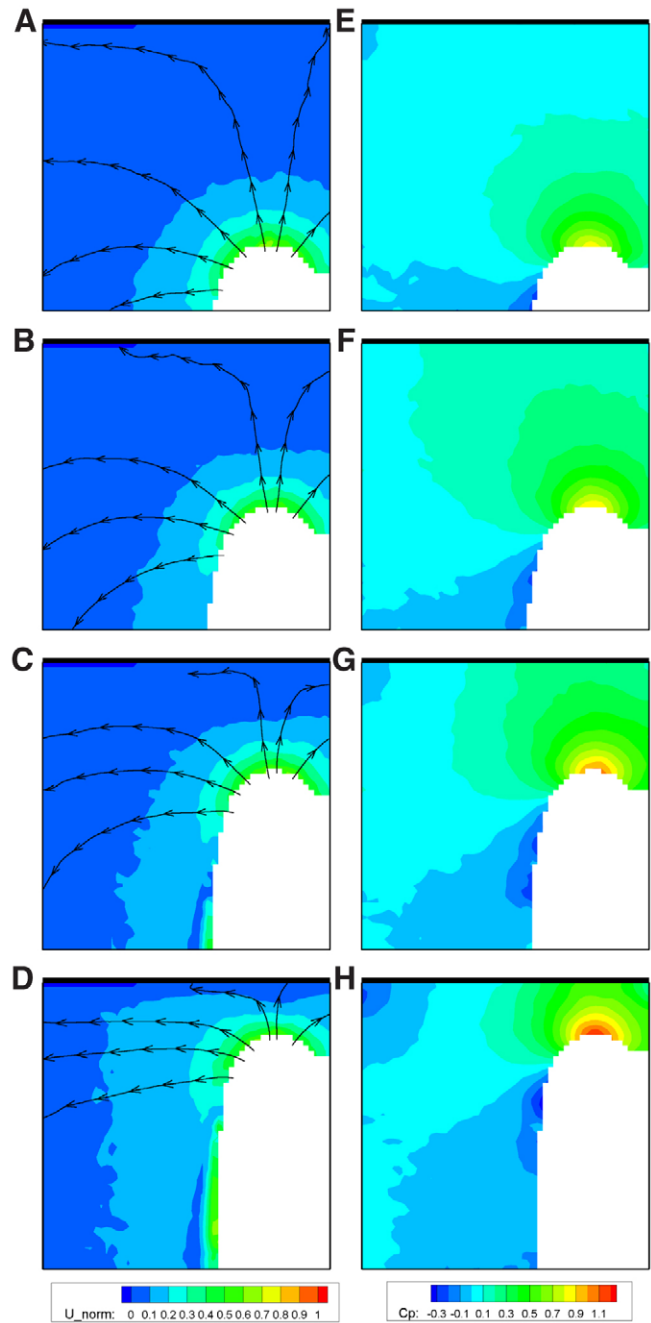

Fig. 8. Flow fields as measured using PIV around a 60 mm blind cave fish at a Re of 3500 approaching a wall at the top of the frame, head-on. (A–D) Normalised velocity (U_{norm}) contours with streamlines in the frame of reference of a stationary observer. The streamlines were drawn from the same points on the body of the fish for each frame. (E–H) Normalised pressure (C_P) contours. Parts of the field on the right hand side of the body were masked out to prevent distortions to the calculated pressure field created by having a very narrow strip of vectors. (A,E) 0.28 BL from the wall (0 s). (B,F) 0.21 BL from the wall (0.07 s). (C,G) 0.13 BL from the wall (0.15 s). (D,H) 0.07 BL from the wall (0.22 s). The fish then started to turn away from the wall to the left, avoiding making any contact with the wall.

background flows in the water, a constant level of random white noise was added to the pressure gradient fields calculated in the CFD models of a 2-D fish shape approaching a wall at Re of 1000 and 2000. Looking at the difference in the canal stimulus relative
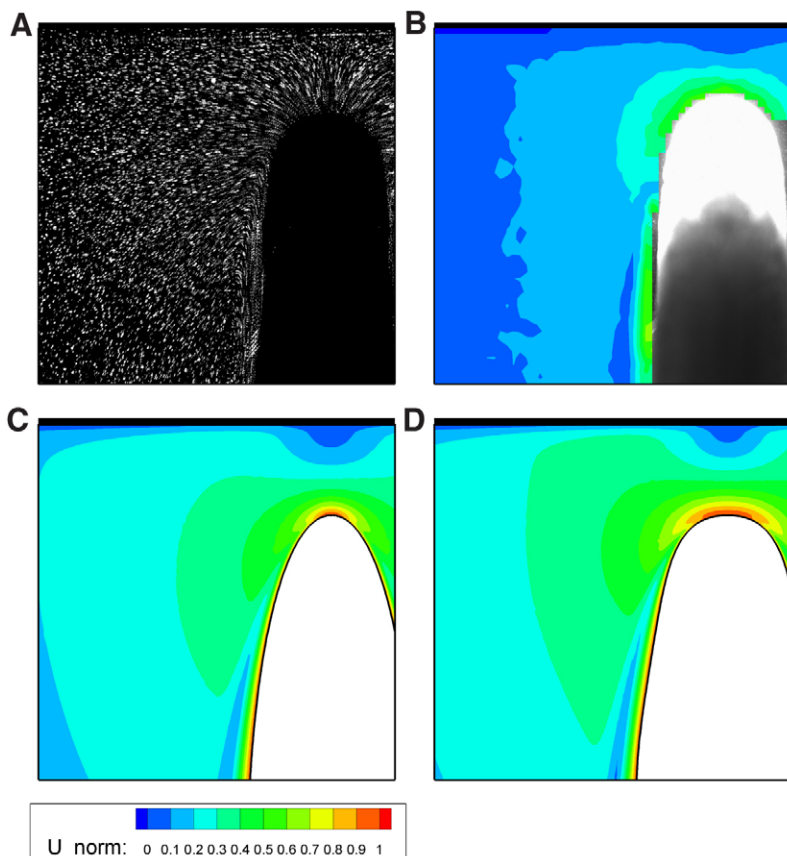
Fig. 9. Comparison of velocity fields from PIV and CFD models, 0.07 BL away from the wall. (A) Artificial particle streak image made by overlaying five consecutive video frames. (B) Normalised velocity (U_{norm}) contours from PIV. Same data as shown in Fig. 8D. (C) Normalised velocity contours for the CFD model of a NACA 0013 aerofoil at a Re of 4000. (D) Normalised velocity contours for the CFD model of a 2-D fish shape at a Re of 4000. All plots of normalised velocity use the same colour scale. The CFD plots are shown in the same orientation as the PIV data to facilitate comparison.

U_norm: 0 0.1 0.2 0.3 0.4 0.5 0.6 0.7 0.8 0.9 1

to the open water stimulus at the nose of the fish as it approached the wall (Fig. 13) showed that, in a given noisy environment, swimming faster improved the signal to noise ratio.

DISCUSSION
General form of the flow fields

The experimental PIV measurements and the CFD models presented here indicate that flow fields around gliding cave fish are similar in many ways to flows around symmetrical aerofoils in uniform flows. Flows around symmetrical aerofoils have stagnation points at the nose and accelerated flow around the widest part of the body, with corresponding high- and low-pressure regions. At high Re, pressure increases over the rear part of the aerofoil to a positive value at the trailing edge. In comparison, at the low Re, which are of interest here, the CFD models showed only a small degree of pressure recovery, with the pressure still being negative at the trailing edge (Fig. 7). These differences are due to the formation of a thick laminar boundary layer at low Re. Other CFD studies of flow around aerofoils at low Re have also found flows dominated by viscous effects and thick laminar boundary layers (Abdo, 2005; Kunz and Kroo, 2001; Mateescu and Abdo, 2004) and are in very good agreement with the results obtained in this study (see Appendix). At the low Re at which most fish swim, viscosity will affect the overall form of the flow field and strongly influence the shear stress and pressure gradient along the body of a fish (Windsor and McHenry, 2009).

The major difference between the open water 2-D and 3-D CFD model results was the much smaller flow acceleration seen at the nose and around the widest part of the body for the 3-D models (Fig. 4). This led to much smaller high- and low-pressure regions, with lower magnitudes (Fig. 5). The smaller accelerations in the 3-

D models were because the fluid had another dimension along which to disperse. The PIV results showed regions of decelerated (high pressure) and accelerated (low pressure) flows around the fish that fell between those seen in the 2-D and 3-D aerofoil models (Figs 4, 5 and 6). This seems consistent with blind cave fish having flattened sides and a greater height than the revolved aerofoil body being modelled in the 3-D case. The body shape of the fish falls somewhere between the infinite wing modelled in the 2-D case, and the torpedo shaped body modelled in the 3-D case. The simplified geometry used in the CFD models means that the calculated flow fields will bound the true flow field around the fish, with the 2-D models having larger changes in the flow and the 3-D models having smaller changes in flow. The numerical accuracy of the models was verified using mesh refinement studies and the resolution of the meshes used was found to give consistent estimates of the flow field around the body (see Appendix for full details).

The pattern of changes in the flow field as fish glided head-on towards a wall measured using PIV were smaller in magnitude than those predicated by the 2-D CFD models (Fig. 9). This is likely to have been because the fluid could move horizontally and vertically around the real fish, whereas in the 2-D models the flow was constrained to move in the horizontal plane, meaning that the fluid between the wall and the nose of the fish had one less dimension to disperse along. Also the PIV measurements did not have sufficient resolution to capture the full details of the stagnation point at the nose of the fish (Fig. 6), where the largest changes in the flow occurred. In addition, the stagnation point may not have been on the plane imaged in some of the PIV trials. In open water the flow fields measured using PIV fell between those calculated in the 2-D and 3-D CFD models. Therefore, if 3-D CFD models were created for the head-on case a
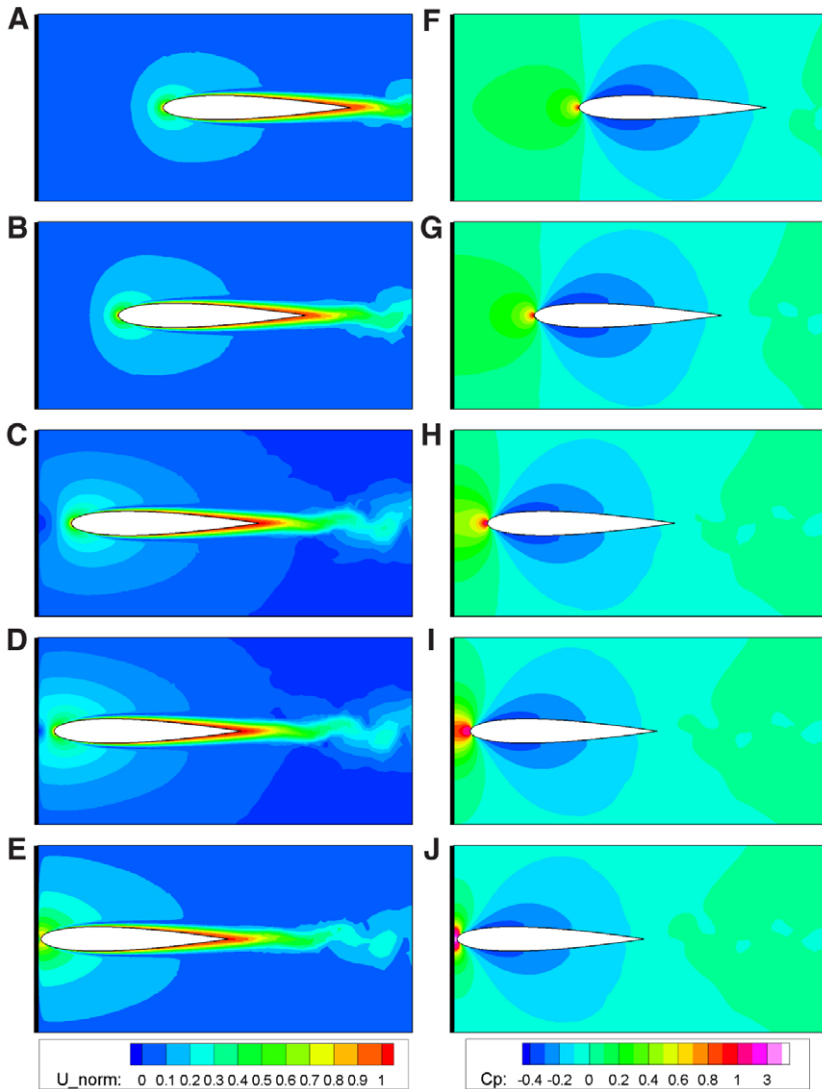
Fig. 10. CFD model solutions for a NACA 0013 aerofoil approaching a wall at a *Re* of 6000. The wall is at the left hand edge of each plot. (A–E) Normalised velocity (U_{norm}) contours. (F–J) Normalised pressure (C_P) contours. (A,F) 0.75 BL from wall. (B,G) 0.50 BL from wall. (C,H) 0.25 BL from wall. (D,I) 0.10 BL from wall. (E,J) 0.02 BL from wall. Vortex shedding occurred from the trailing edge of the NACA 0013 and fish-shaped models at a *Re* of 6000, but not at lower *Re*. A valid mesh was not possible at distances closer than 0.02 BL to the wall.

similar result might be expected. However, it seems likely that the real-world flow would be closer to the 3-D CFD model, as the shape of the nose of a blind cave fish is very similar to the shape of the nose of the body of revolution used in the 3-D CFD models.

Lateral line stimuli

The location of the neuromasts of the lateral line is well suited to measure the flow field around a gliding blind cave fish (Fig. 14). The stimulus to the lateral line was greatest at the head of the fish. The highest pressure occurred at the stagnation point right at the tip of the snout of the fish, with the greatest pressure gradient being slightly to either side of the snout (Fig. 7). The mandibular, supraorbital and infraorbital canals run close to the tip of the snout (Schemmel, 1967) but there are no canal pores right at the tip, so the pressure at the stagnation point will not be sampled; but there are pores close by in these canals which should capture the peak in the pressure gradient. The peak shear stress was located slightly to either side of the snout (0.025 BL for the 3-D model). The superficial neuromasts associated with the mandibular, supraorbital and infraorbital canals are well positioned to be stimulated by the peak shear stress. When fish approached a wall head-on, the largest changes in lateral line stimuli occurred where the stimuli were

maximal in open water (Fig. 11). The neuromasts that were most strongly stimulated in open water would also experience the greatest change in stimulation as the fish approached a wall head-on.

Comparing the results for the 2-D aerofoil and fish shape models (Fig. 7) showed that small differences in the shape of a body had a noticeable impact on the shape of the pressure and shear distributions on that body. Given the complex geometry of the body of a fish, with surface features such as the nasal nares and structures such as the operculum, it seems likely that the flow field will have an added degree of complexity in the regions around these features. The effects of this complex geometry would need to be taken into account by the fish when processing the stimuli encoded by the lateral line.

The mathematical models of Hassan (Hassan, 1992a; Hassan, 1992b) give a good indication that there is a wealth of information in the flow field around a gliding fish. However, as the results presented here show, the flow around a gliding fish is strongly influenced by viscous effects, meaning that the stimuli predicted by Hassan's inviscid models will be inaccurate. In comparison with the 3-D body gliding in open water (Fig. 7), Hassan's model seems to overestimate the negative pressure peak, and predict positive pressures down the rear part of the fish, in contrast to
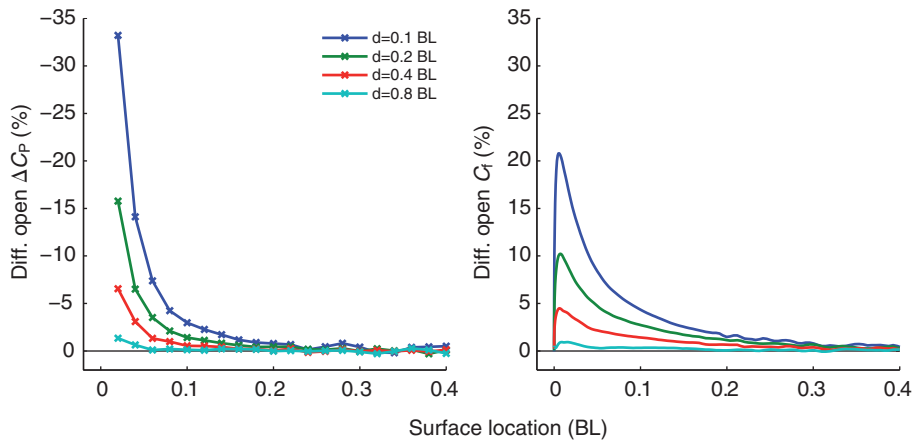
Fig. 11. Difference between the lateral line stimuli for a NACA 0013 aerofoil as it approached a wall head-on at a *Re* of 6000 and the open water stimuli at the same *Re*. Differences given as a percentage of the maximum C_P and C_f values in open water. Only the difference in the stimuli along the first 0.4 BL are shown for clarity; the differences in stimuli down the rest of the body were very small. As the body moved closer to the wall the peak in the stimuli near the nose increased rapidly. The differences in stimuli for a representative selection of distances (*d*) are shown. (A) Difference in normalised pressure differences across canal pores from when in open water. (B) Difference in normalised shear stress from when in open water.

the negative pressures seen in this study. Hassan's results are similar to the flows seen around aerofoils at high *Re*, which is consistent with the inviscid assumption used in the models. This comparison indicates that, in order to accurately model the flow field around fish moving at low *Re*, the effects of viscosity need to be included.

Detecting a wall

A blind cave fish approaching a wall head-on needs to sense the change in the flow field around its body caused by the presence of the wall in order to be able to detect the wall. Therefore, the sensory task is to detect a change in lateral line stimuli, not merely the presence or absence of stimuli. It has been found for many different sensory modalities, in many species, that the smallest change in a stimulus that can be detected is directly proportional to the magnitude of the original stimulus (Schiffman, 1996; Teghtsoonian, 1971). In other words, there is a minimum relative change in the stimulus that can be detected (e.g. 10%); this is known as the Weber fraction or the just noticeable difference (JND). For the lateral line in general, and blind cave fish in particular, measurements of the Weber fraction are not readily available. Based on previous behavioural work, blind cave fish approaching a wall head-on react to the wall at a mean distance of approximately 0.10 BL (Windsor et al., 2008). Based on the 2-D head-on CFD models at a distance of 0.10 BL the maximum change in the canal stimuli relative to open water was 33% and for the superficial stimuli 21% (Fig. 11). The 2-D modelling results are

an over-estimate of the change in the stimulus to the lateral line as the flow can move both horizontally and vertically around the nose of the fish as it approaches a wall. As such, direct comparisons to experimental data on the sensitivity of the lateral line (e.g. Gorner, 1963; Kroese and Schellart, 1992; Kroese et al., 1978; van Netten, 2006) are not possible because the magnitude of the lateral stimulus estimated from the 2-D models will be much greater than for the real flow. The pattern of changes in the flow as the fish approaches the wall modelled in the 2-D case, however, can be expected to be similar to those in the real case, as shown by comparing the PIV and CFD results (Figs 8 and 10).

Effect of swimming speed

The CFD models showed that, over the behaviourally relevant range of *Re*, there was a small decrease in the distance at which a certain relative change in lateral line stimuli occurred as *Re* increased (Fig. 12). This means that if it is assumed that the fish are sensitive to a certain relative change in lateral line stimulus (JND), then fish should detect walls in front of them at roughly the same distance irrespective of their swimming speed. This agrees with previous behavioural experiments (Windsor et al., 2008) that found no significant correlation between the distance at which cave fish reacted when approaching a wall head-on and their swimming speed.
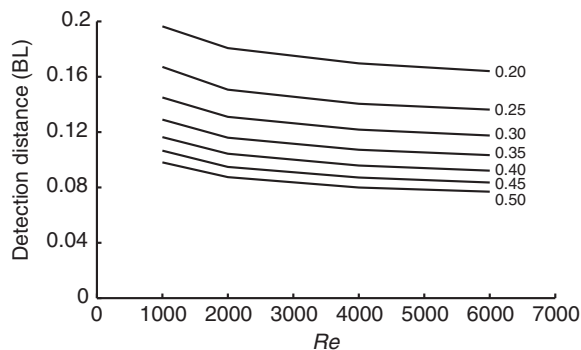

Fig. 12. Effect of *Re* on the distance that a fish would detect the wall, assuming the fish responded to a certain relative change in canal lateral line stimuli. Sensitivity thresholds are labelled on the graph. Results from the fish-shaped CFD model.
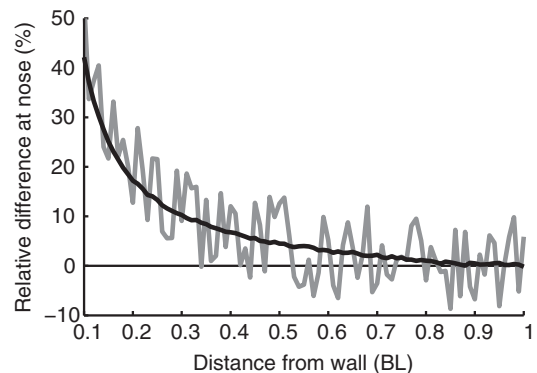

Fig. 13. Effect of a set level of environmental noise on the relative difference in pressure across the canal pores closest to nose of a NACA 0013 aerofoil at different *Re*. Random white noise with a maximum magnitude of 10% of the open water pressure difference at a *Re* of 1000 was added to both sets of CFD results. The grey line is at a *Re* of 1000, the black line is at a *Re* of 2000.
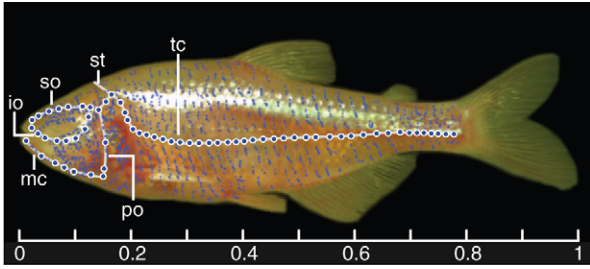
Fig. 14. Diagram of the lateral line of blind cave fish (*Astyanax fasciatus*). Large blue circles with white outlines represent canal pores; canals are shown with white lines. A canal neuromast is located approximately midway between each pair of pores. The approximate locations of the superficial neuromasts are shown with small blue dots. io, infraorbital canal; mc, mandibular canal; po, preopercular canal; so, supraorbital canal; st, supratemporal canal; tc, trunk canal. The scale bar represents one body length. Based on anatomical drawings from Schemmel (Schemmel, 1967).

Blind cave fish have been shown to increase their swimming speed in unfamiliar environments (Teyke, 1985; Teyke, 1988) and the duration of this speed increase was found to be related to the symmetry of the environment and whether the fish has any previous experience in the environment (Teyke, 1989). Therefore, it has previously been assumed that by swimming faster blind cave fish enhance their ability to detect their surroundings in some way. This study found that at higher swimming speeds (higher *Re*) the predicted detection distance actually decreased. This apparent disagreement may be reconciled if the effects of environmental noise are considered. The experiments and models presented here and in previous behavioural studies (Windsor et al., 2008) were all conducted in still water with no environmental noise. In the absence of environmental noise then the relative change in the stimulus to the lateral line is only weakly affected by swimming speed (Fig. 12). But if a set level of random white noise is added to the lateral line stimulus then at higher swimming speeds the signal to noise ratio will be greater (Fig. 13) and it should be easier for the fish to detect the change in the stimuli created by the presence of a wall. This hypothesis remains to be tested experimentally, but could explain why blind cave fish swim faster when introduced into unfamiliar environments. Another alternative hypothesis is that the fish may simply swim faster in order to reduce the time that it takes to explore a new environment.

APPENDIX
Computational fluid dynamic methods

The CFD modelling was done with the ALE CFD code (Norris et al., 2010; Were, 1997), which solves the incompressible Navier–Stokes equations on an unstructured Voronoi finite volume mesh, using a cell-centred collocated formulation. The steady flow calculations for the open water models used the SIMPLE algorithm (Patankar and Spalding, 1972) modified for a collocated mesh. The transient calculations used in the head-on models used a non-staggered adaptation of the MAC method (Harlow and Welch, 1965), using an ALE formulation (Hirt et al., 1974) adapted to a Voronoi mesh (Norris et al., 2010). For both types of models Rhie–Chow velocity interpolation (Rhie and Chow, 1983) was used along with second order differencing for diffusion, the third order accurate QUICK scheme (Leonard, 1979) for advection, and first order explicit differencing in time. The models were considered to have iteratively converged when the change between each iteration was reduced by six orders of magnitude. The flow

in all models was assumed to be laminar, given the low *Re* being modelled.

Verification of open water 2-D computational fluid dynamic models

To verify the open water 2-D CFD models, a mesh refinement study was conducted based on a NACA 0008 aerofoil in uniform flow at a *Re* of 6000. This aerofoil was used in order to be able to compare the results with those of other studies (Abdo, 2005; Kunz and Kroo, 2001; Mateescu and Abdo, 2004). Three different meshes were used, with 128, 256 and 512 nodes along the aerofoil. The mesh spacing at the edges of the domain and the inflation layer spacing were both adjusted in proportion to the number of nodes along the aerofoil.

Richardson extrapolation (Celik, 2008) was used to calculate the observed order of convergence and to estimate the discretisation errors involved with different mesh resolutions (Table A1). The gradient of the normalised pressure (∇C_P) at half chord length were used as a measure of the shape of the pressure distribution. The gradient was calculated by fitting a straight line to the pressure and shear values between 0.45 and 0.55 BL, using a least squares method. The normalised shear stress (C_f) at the position of the peak shear stress on the highest resolution mesh was used as a measure of the shape of the shear stress distribution. Both measures reached asymptotic convergence with an order of convergence of 2.31 and 2.72, respectively, and estimated errors, given by the grid convergence index (GCI), of 1.18 and 3.13%. This order of convergence is slightly below the formal third order of convergence of the QUICK differencing scheme, but this may be due to the diffusion terms being only second order accurate (Leonard, 1988) and so this is not unexpected.

To test the effect of domain size the NACA 0013 2-D aerofoil model was run at a *Re* of 6000 with a domain size of 20×20 BL, twice that of the standard models. The same mesh resolution was used as for the 256-node mesh with the smaller domain size. With the larger domain size the maximum velocity in the flow decreased by 0.24%, indicating that the proximity of the domain boundaries had little significant effect on the flow distribution around the aerofoil.

For the full CFD study, a mesh with 256 nodes along the aerofoil was selected as a reasonable compromise between accuracy and computation time, giving a good measurement of the flow distribution around the aerofoil. With this mesh resolution and 20 inflation layers around the body there were at least 20 nodes within the thinnest part of the boundary layer in all trials. The models were

Table A1. Mesh refinement study results for a NACA 0008 aerofoil at a Reynolds number of 6000 in open water

Mesh (N)	∇C_P at 0.5 BL	C_f at 0.0065 BL
128 (20782)	0.288	0.147
256 (83874)	0.300	0.171
512 (445725)	0.302	0.175
Relative error (%)	3.78	14.2
Order of convergence	2.31	2.72
GCI (%)	1.18	3.13

N, total number of nodes in each mesh; ∇C_P, gradient of the normalised pressure; C_f, skin friction coefficient, calculated at the position of the peak value, which was calculated using the highest resolution mesh; BL, body lengths.

The relative error and grid convergence index (GCI) were calculated based on the mesh with 256 nodes along the body that was used in the full computational fluid dynamics study.
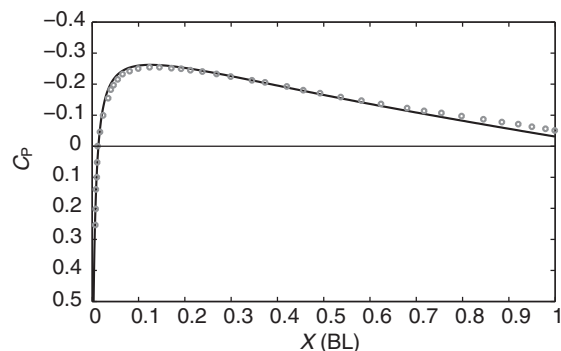
Fig. A1. Normalised pressure distribution on a NACA 0008 aerofoil at a *Re* of 6000. Black line, arbitrary Lagrangian–Eulerian CFD solution; grey circles, data from Mateescu and Abdo (Mateescu and Abdo, 2004). *X*, distance along chord; BL, body length.

Table A2. Mesh refinement study results for an axisymmetric body of revolution based on a NACA 0013 aerofoil at a Reynolds number of 6000 in open water

Mesh (*N*)	∇C_P at 0.5 BL	C_f at 0.02 BL
85 (38507)	0.202	0.0815
128 (102897)	0.226	0.109
196 (276870)	0.234	0.123
Relative error (%)	10.5	25.5
Order of convergence	3.29	2.24
GCI (%)	6.79	29.4

N, total number of nodes in each mesh; ∇C_P, gradient of the normalised pressure; C_f, skin friction coefficient, calculated at the position of the peak value, which was calculated using the highest resolution mesh; BL, body lengths.
The relative error and the grid convergence index (GCI) were calculated based on the mesh with 128 nodes along the body that was used in the full computational fluid dynamics study.

run serially on a Linux cluster with 3.0 GHz Pentium D processors, with each model typically taking around 3 h to run. Models with 512 nodes along the aerofoil took approximately 100 h to solve. The pressure distributions obtained compared well with other published CFD pressure distributions available for this *Re* range (Fig. A1) (Mateescu and Abdo, 2004).

Verification of open water 3-D computational fluid dynamic models

To verify the open water 3-D CFD models a mesh refinement study was conducted using an axisymmetric body of revolution based on a NACA 0013 aerofoil, in a uniform flow at a *Re* of 6000. Three different meshes were used with 85, 128 and 192 nodes along the body. Using the same methodology as the 2-D case, Richardson extrapolation was used to calculate the observed order of convergence and to estimate the discretisation errors involved with different mesh resolutions (Table A2). The pressure distribution was asymptotically converging with an observed order of convergence of 3.29 and an estimated error (GCI) of 6.79%. This order of convergence is above the formal order of the QUICK differencing scheme, indicating that the mesh resolution around the aerofoil increased by a higher factor than predicted by the measure of global mesh size used in the mesh refinement calculations. The shear stress distribution was converging (order of convergence 2. 24), but the peak shear stress estimated error (GCI) was still large at 29.4%.

For the full CFD study, a mesh with 128 nodes along the body was selected as a reasonable compromise between accuracy and computational cost, giving a good estimate of the pressure distribution around the aerofoil, while giving an indication of the shape of the shear distribution. The 128-node models took approximately 3 h to solve, and the 192-node mesh took over 60 h to solve. It was felt that the 128-node mesh gave a good picture of the general characteristic of the flow field around a 3-D body of revolution and allowed the questions of interest to be addressed.

Verification of head-on computational fluid dynamic models

To verify the implementation of the ALE-based moving mesh, the flow field calculated around a NACA 0013 aerofoil at a *Re* of 6000 was examined using both a stationary and a moving mesh. The moving mesh model essentially represented an aerofoil being impulsively started from rest, so it was expected that it would take some time for the transient effects of the sudden acceleration to fade. The aerofoil was moved through 9 BL and the results showed that after it had moved

4 BL the pressure field was nearly identical to that modelled on the stationary mesh. As the aerofoil moved from 4 to 9 BL, the pressure distribution on the aerofoil was essentially constant. This indicated that in the head-on models the flow field around the body would be reasonably steady by the time the body had moved 4 BL, and that over the final 2 BL, as it approached the wall, any changes to the flow field were due to the presence of the wall.

The effect of the time step used in the moving mesh model was tested using a time step refinement study with a NACA 0013 aerofoil at a *Re* of 6000, and results were compared at a distance of 0.10 BL from the wall. Richardson extrapolation was used to calculate the observed order of convergence and to estimate the discretisation errors involved with the size of the time step (Table A3). The pressure distribution showed oscillating convergence with an observed order of convergence of 2.01 and an estimated error (GCI) of 3.47%. The shear stress distribution had not yet converged (order of convergence 0.271) and had an estimated error (GCI) of 9.36%.

For the full CFD study a time step of 4×10^{-4} was selected as giving a good estimate of the pressure distribution around the aerofoil, while giving an indication of the shape of the shear distribution. It was felt that this time step gave a good picture of the general characteristics of the flow field around the body and allowed the questions of interest to be addressed. The use of this time step ensured that the maximum Courant number was always less than 0.4, maintaining the stability and accuracy of the solution.

Table A3. Time step refinement study results for a NACA 0013 aerofoil moving at a Reynolds number of 6000 when 0.1 body lengths away from the wall

Time step	∇C_P at 0.5 BL	C_f at 0.016 BL
8×10^{-4}	0.385	0.147
4×10^{-4}	0.420	0.149
2×10^{-4}	0.411	0.151
Relative error (%)	8.39	1.55
Order of convergence	2.01	0.271
GCI (%)	3.47	9.36

∇C_P, gradient of the normalised pressure; C_f, skin friction coefficient, calculated at the position of the peak value, which was calculated using the highest resolution time step; BL, body lengths.
The relative error and the grid convergence index (GCI) were calculated based on the 4×10^{-4} time step that was used in the full computational fluid dynamics study.

LIST OF SYMBOLS AND ABBREVIATIONS

ALE	arbitrary Lagrangian–Eulerian
BL	body length
CFD	computational fluid dynamics
C_f	skin friction coefficient
C_P	coefficient of pressure
P	pressure field
PIV	particle image velocimetry
Re	Reynolds number
$\mathbf{u}$	velocity field
$\mathbf{u}_t$	tangential velocity
U	swimming speed of the fish
U_{norm}	normalised velocity field
y	direction normal to the surface
ΔC_P	normalised pressure difference across canal pores
∇C_P	gradient of the normalised pressure
μ	the dynamic viscosity of the fluid
ρ	the density of the fluid
τ_w	wall shear stress

REFERENCES

Abdo, M. (2005). Low-Reynolds number aerodynamics of airfoils at incidence. In *3rd AIAA Aerospace Sciences Meeting and Exhibit*. Reno, Nevada: American Institute of Aeronautics and Astronautics.

Anderson, J. D. (1995). *Computational Fluid Dynamics: the Basics with Applications.* New York, Bogotá: McGraw-Hill.

Cameron, S. M. (2007). *Near-Boundary Flow Structure and Particle Entrainment.* PhD Thesis, University of Auckland, NZ.

Celik, I. B. (2008). Procedure for estimation and reporting of uncertainty due to discretization in CFD applications. *J. Fluid. Eng.* **130**, 078001.

Coombs, S. and Montgomery, J. C. (1999). The enigmatic lateral line system. In *Comparative Hearing: Fish and Amphibians* (ed. R. R. Fay and A. N. Popper), pp. 319-362. New York: Springer-Verlag.

Denton, E. J. and Gray, J. (1983). Mechanical factors in the excitation of clupeid lateral lines. *Proc. R. Soc. Lond. B. Biol. Sci.* **218**, 1-26.

Denton, E. J. and Gray, J. (1988). Mechanical factors in the excitation of the lateral line of fishes. In *Sensory Biology of Aquatic Animals* (ed. J. Atema, R. R. Fay, A. N. Popper and W. N. Tavolga), pp. 595-618. New York: Springer-Verlag.

Dijkgraaf, S. (1963). Functioning and significance of lateral-line organs. *Biol. Rev. Camb. Philos. Soc.* **38**, 51-105.

Drucker, E. G. and Lauder, G. V. (2002). Experimental hydrodynamics of fish locomotion: Functional insights from wake visualization. *Integr. Comp. Biol.* **42**, 243-257.

Dubois, A. B., Cavagna, G. A. and Fox, R. S. (1974). Pressure distribution on body surface of swimming fish. *J. Exp. Biol.* **60**, 581-591.

Fujisawa, N., Nakamura, K. and Srinivas, K. (2004). Interaction of two parallel plane jets of different velocities. *J. Visual.* **7**, 135-142.

Fujisawa, N., Tanahashi, S. and Srinivas, K. (2005). Evaluation of pressure field and fluid forces on a circular cylinder with and without rotational oscillation using velocity data from PIV measurement. *Meas. Sci. Technol.* **16**, 989-996.

Fujisawa, N., Nakamura, Y., Matsuura, F. and Sato, Y. (2006). Pressure field evaluation in microchannel junction flows through mu PIV measurement. *Microfluidics and Nanofluidics* **2**, 447-453.

Gorner, P. (1963). Untersuchungen zur morphologie und elektrophysiologie des seitenlinienorgans vom krallenfrosch (*Xenopus laevis* Daudin). *Zeitschrift Fur Vergleichende Physiologie* **47**, 316-338.

Gurka, R., Liberzon, A., Hefetz, D., Rubinstein, D. and Shavit, U. (1999). Computation of pressure distribution using PIV velocity data. In *Proceedings of the Third International Workshop PIV*, pp. 671-676. Santa Barbara.

Harlow, F. H. and Welch, J. E. (1965). Numerical calculation of time-dependent viscous incompressible flow of fluid with free surface. *Phys. Fluids* **8**, 2182-2189.

Hassan, E. S. (1985). Mathematical-analysis of the stimulus for the lateral line organ. *Biol. Cybern.* **52**, 23-36.

Hassan, E. S. (1989). Hydrodynamic imaging of the surroundings by the lateral line of the blind cave fish *Anoptichthys jordani*. In *The Mechanosensory Lateral Line: Neurobiology and Evolution* (ed. S. Coombs, P. Gorner and H. Munz), pp. 217-228. New York: Springer-Verlag.

Hassan, E. S. (1992a). Mathematical-description of the stimuli to the lateral line system of fish derived from a 3-dimensional flow field analysis: I. The cases of moving in open water and of gliding towards a plane surface. *Biol. Cybern.* **66**, 443-452.

Hassan, E. S. (1992b). Mathematical-description of the stimuli to the lateral line system of fish derived from a 3-dimensional flow field analysis: II. The case of gliding alongside or above a plane surface. *Biol. Cybern.* **66**, 453-461.

Hirt, C. W., Amsden, A. A. and Cook, J. L. (1974). An arbitrary Lagrangian-Eulerian computing method for all flow speeds. *J. Comput. Phys.* **14**, 227-253.

Hosokawa, S., Moriyama, S., Tomiyama, A. and Takada, N. (2003). PIV measurement of pressure distributions about single bubbles. *J. Nucl. Sci. Technol.* **40**, 754-762.

Jielof, R., Spoor, A. and Devries, H. (1952). The microphonic activity of the lateral line. *J. Physiol. Lond.* **116**, 137-157.

Kalmijn, A. J. (1988). Hydrodynamic and acoustic field detection. In *Sensory Biology of Aquatic Animals* (eds J. Atema, R. R. Fay, A. N. Popper and W. N. Tavolga), pp. 83-130. New York: Springer-Verlag.

Kalmijn, A. J. (1989). Functional evolution of lateral line and inner ear sensory systems. In *The Mechanosensory Lateral Line: Neurobiology and Evolution* (eds S. Coombs, P. Gorner and H. Munz), pp. 187-216. New York: Springer-Verlag.

Kroese, A. B. A. and Schellart, N. A. M. (1992). Velocity-sensitive and acceleration-sensitive units in the trunk lateral line of the trout. *J. Neurophysiol.* **68**, 2212-2221.

Kroese, A. B. A., Vanderzalm, J. M. and Vandenbercken, J. (1978). Frequency-response of lateral-line organ of *Xenopus laevis*. *Pflugers Arch. Eur. J. Physiol.* **375**, 167-175.

Kuiper, J. W. (1967). Frequency characteristics and functional significance of the lateral line organ. In *Lateral Line Detectors* (ed. P. H. Cahn), pp. 105-121. Bloomington: Indiana University Press.

Kunz, P. J. and Kroo, I. (2001). Analysis and design of airfoils for use at ultra-low Reynolds numbers. In *Fixed and Flapping Wing Aerodynamics For Micro Air Vehicle Applications*, Vol. 195 (ed. T. J. Mueller), pp. 35-60. Reston, VA: American Institute of Aeronautics and Astronautics.

Leonard, B. P. (1979). Stable and accurate convective modeling procedure based on quadratic upstream interpolation. *Comput. Meth. Appl. Mech. Eng.* **19**, 59-98.

Leonard, B. P. (1988). Elliptic systems: finite-difference method IV. In *Handbook of Numerical Heat Transfer* (eds W. J. Minkowycz, E. M. Sparrow, G. E. Schneider and R. H. Pletcher), pp. 347–378. New York: Wiley.

Mateescu, D. and Abdo, M. (2004). Aerodynamic analysis of airfoils at very low Reynolds numbers. In *42nd AIAA Aerospace Sciences Meeting and Exhibit*, pp. 6341-6351. Reno, NV, USA: American Institute of Aeronautics and Astronautics Incorporated, Reston.

McHenry, M. J., Strother, J. A. and van Netten, S. M. (2008). Mechanical filtering by the boundary layer and fluid-structure interaction in the superficial neuromast of the fish lateral line system. *J. Comp. Physiol. A* **194**, 795-810.

Murai, Y., Nakada, T., Suzuki, T. and Yamamoto, F. (2007). Particle tracking velocimetry applied to estimate the pressure field around a Savonius turbine. *Meas. Sci. Technol.* **18**, 2491-2503.

Norris, S. E., Were, C. J., Richards, P. J. and Mallinson, G. D. (2010). A Voronoi based ALE solver for the calculation of incompressible flow on deforming unstructured meshes. *Int. J. Numer. Meth. Fluid.* Epub ahead of print.

Partridge, B. L. and Pitcher, T. J. (1980). The sensory basis of fish schools - relative roles of lateral line and vision. *J. Comp. Physiol.* **135**, 315-325.

Patankar, S. V. and Spalding, D. B. (1972). Calculation procedure for heat, mass and momentum-transfer in 3-dimensional parabolic flows. *Int. J. Heat Mass Transf.* **15**, 1787-1806.

Rapo, M. A., Jiang, H., Grosenbaugh, M. and Coombs, S. (2009). Using computational fluid dynamics to calculate the stimulus to the lateral line of a fish in still water. *J. Exp. Biol.* **212**, 1494-1505.

Rhie, C. M. and Chow, W. L. (1983). Numerical study of the turbulent-flow past an airfoil with trailing edge separation. *AIAA J.* **21**, 1525-1532.

Roache, P. J. (1997). Quantification of uncertainty in computational fluid dynamics. *Annu. Rev. Fluid Mech.* **29**, 123-160.

Schemmel, C. (1967). Vergleichende Untersuchungen an den Hautsinnesorganen ober- und unterirdisch lebender Astyanax-Formen. *Zeitschrift fur Morphologie der Tiere* **61**, 255-316.

Schiffman, H. R. (1996). *Sensation and Perception: an Integrated Approach.* New York: Wiley.

Schlicke, T., Cameron, S. M. and Coleman, S. E. (2007). Galvanometer-based PIV for liquid flows. *Flow. Meas. Instrum.* **18**, 27-36.

Teghtsoonian, R. (1971). On the exponents in Stevens' law and the constant in Ekman's law. *Psychol. Rev.* **78**, 71-80.

Teyke, T. (1985). Collision with and avoidance of obstacles by blind cave fish *Anoptichthys jordani* (Characidae). *J. Comp. Physiol. A* **157**, 837-843.

Teyke, T. (1988). Flow field, swimming velocity and boundary layer: parameters which affect the stimulus for the lateral line organ in blind fish. *J. Comp. Physiol. A* **163**, 53-61.

Teyke, T. (1989). Learning and remembering the environment in the blind cave fish *Anoptichthys jordani*. *J. Comp. Physiol. A* **164**, 655-662.

Teyke, T. (1990). Morphological differences in neuromasts of the blind cave fish *Astyanax hubbsi* and the sighted river fish *Astyanax mexicanus*. *Brain Behav. Evol.* **35**, 23-30.

van Netten, S. M. (2006). Hydrodynamic detection by cupulae in a lateral line canal: functional relations between physics and physiology. *Biol. Cybern.* **94**, 67-85.

von Campenhausen, C., Riess, I. and Weissert, R. (1981). Detection of stationary objects by the blind cave fish *Anoptichthys jordani* (Characidae). *J. Comp. Physiol. A* **143**, 369-374.

Weissert, R. and von Campenhausen, C. (1981). Discrimination between stationary objects by the blind cave fish *Anoptichthys jordani* (Characidae). *J. Comp. Physiol. A* **143**, 375-381.

Were, C. J. (1997). *The Free-ALE Method for Unsteady Incompressible Flow in Deforming Geometries.* PhD Thesis, University of Auckland, NZ.

White, F. M. (2006). *Viscous Fluid Flow.* Boston: McGraw-Hill.

Windsor, S. P. (2008). *Hydrodynamic Imaging by Blind Mexican Cave Fish.* PhD Thesis, University of Auckland, NZ.

Windsor, S. P. and McHenry, M. J. (2009). The influence of viscous hydrodynamics on the fish lateral-line system. *Integr. Comp. Biol.* **49**, 691-701.

Windsor, S. P., Tan, D. and Montgomery, J. C. (2008). Swimming kinematics and hydrodynamic imaging in the blind Mexican cave fish (*Astyanax fasciatus*). *J. Exp. Biol.* **211**, 2950-2959.

Windsor, S. P., Norris, S. E., Cameron, S. M., Mallinson, G. D. and Montgomery, J. C. (2010). The flow fields involved in hydrodynamic imaging by blind Mexican cave fish (*Astyanax fasciatus*). Part II: gliding parallel to a wall. *J. Exp. Biol.* **213**, 3832-3842.

Wolfgang, M. J., Anderson, J. M., Grosenbaugh, M. A., Yue, D. K. P. and Triantafyllou, M. S. (1999). Near-body flow dynamics in swimming fish. *J. Exp. Biol.* **202**, 2303-2327.

Yasuda, K. (1973). Comparative studies on swimming behavior of blind cave fish and goldfish. *Comp. Biochem. Physiol.* **45**, 515-527.